J. Math. Biol. (2015) 71:533–550
DOI 10.1007/s00285-014-0827-2

Mathematical Biology

Conformal mapping in optical biosensor applications

Matthew E. Zumbrum · David A. Edwards

Received: 7 November 2013 / Revised: 13 June 2014 / Published online: 10 September 2014

Abstract Optical biosensors are devices used to investigate surface-volume reaction kinetics. Current mathematical models for reaction dynamics rely on the assumption of unidirectional flow within these devices. However, new devices, such as the Flexchip, include a geometry that introduces two-dimensional flow, complicating the depletion of the volume reactant. To account for this, a previous mathematical model is extended to include two-dimensional flow, and the Schwarz–Christoffel mapping is used to relate the physical device geometry to that for a device with unidirectional flow. Mappings for several Flexchip dimensions are considered, and the ligand depletion effect is investigated for one of these mappings. Estimated rate constants are produced for simulated data to quantify the inclusion of two-dimensional flow in the mathematical model.

Keywords Flexchip · Optical biosensors · Perturbation methods · Schwarz–Christoffel mapping · Surface-volume reactions

Mathematics Subject Classfication 35C20 · 92C45

1 Introduction

Optical biosensors are devices used to measure rate constants via surface-volume reactions. In this type of reaction, one reactant (the ligand) is dissolved in a fluid which flows over a surface on which another reactant (the bound ligand or receptor) is confined in a reacting zone. Biosensor devices measure and average the change in the bound

M. E. Zumbrum (✉)
Department of Mathematics, Temple University, Philadelphia, PA 19122, USA
e-mail: zumbrum@temple.edu

D. A. Edwards
Department of Mathematical Sciences, University of Delaware, Newark, DE 19716, USA

ligand concentration for a reacting zone to obtain a quantity known as a sensogram for the average bound ligand concentration (GE Healthcare 2007). From this output, association and dissociation rate constants for a particular reaction can be calculated.

Due to the physical setup, reactants are not well mixed, making it important to consider transport within the system. Upstream reactions deplete available ligand at downstream receptors, slowing the reaction and decreasing the average bound ligand concentration. Ignoring transport effects could lead to the underestimation of rate constants for a particular interaction.

Mathematical models have been developed for surface-volume reactions to determine the effect of transport within this system. Edwards (1999) develops the standard two-compartment model for the experimental injection phase, in which a uniform ligand concentration is used in the device. A system of partial differential equations (PDE) for the ligand concentration and bound ligand concentrations includes the dimensionless Damköhler number to incorporate transport effects related to physical parameters. For the reaction-limited problem, this system may be replaced with a simpler nonlinear ordinary differential equation (ODE) using perturbation methods (Edwards 2001; Mason et al. 1999). This differential equation, called an effective rate constant (ERC) equation, models the average bound ligand concentration over a reacting zone.

A key modeling assumption which allows for analytical results is that flow within biosensor devices is unidirectional (Edwards 2011). However, two-dimensional flow occurs within some devices, such as the hexagonal Biacore Flexchip (Rich et al. 2008), for which we display a schematic representation in Fig. 1. The Flexchip includes a rectangular array of reacting zones over which the solution flows from the inlet on the left to the outlet on the right.

To better quantify ligand depletion within this device, we extend previous one-dimensional results for the Flexchip (Edwards 2011) to the case of two-dimensional flow. Using conformal mapping techniques, we then examine how considering the flow to be two-dimensional affects the ligand concentration in the Flexchip. Using the Schwarz–Christoffel mapping, we map the infinite strip to a trapezoid representing half of the Flexchip, exploiting the symmetry of the device, and extend results from the one-dimensional case to the two-dimensional case. Upon deriving results for a general trapezoid, we include examples for several mappings of possible Flexchip dimensions and compare ligand depletion within the Flexchip for one of these examples. We take this analysis a step further by simulating sensogram data using the two-dimensional flow model and fitting the model for one-dimensional flow to this simulated data to produce estimated rate constants. Comparing these estimated values with the actual values used to produce the simulated data, we quantify the effect of ignoring two-dimensional flow.

2 Model background

Generalizing the unidirectional flow model, we derive the velocity profile for two-dimensional parallel flow between the channel floor and ceiling, and discuss the injection phase model for the three-dimensional two-compartment model for ligand and bound ligand concentrations. Using a boundary layer at the reacting surface and

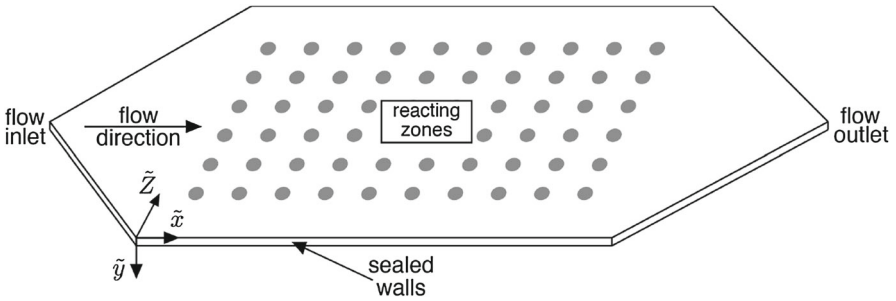

Fig. 1 Three-dimensional schematic representation of the Flexchip. Note that $\tilde{y}$ points down, so the reacting zones are at $\tilde{y} = 0$. Also note the choice of notation $\tilde{Z}$ to minimize confusion with the complex variable z used in the conformal mapping procedure

a reaction time scale, we obtain the leading-order bound state and an expression for the ligand concentration via perturbation methods.

2.1 Velocity profile

For biosensor devices, the height of the channel $\tilde{H}$ is much smaller than the length $\tilde{L}$ and width $\tilde{W}$ (see Fig. 1). This aspect ratio is consistent with a Hele-Shaw flow. A detailed analysis is performed in Edwards (2011); we summarize the results here for our purposes.

If we let $\tilde{V}$ be the characteristic velocity of the flow, then in the Flexchip, the Reynolds number $\mathrm{Re} = \tilde{\rho}\tilde{V}\tilde{H}^2/\tilde{\mu}\tilde{L} \ll 1$. Here $\tilde{\rho}$ is the fluid density and $\tilde{\mu}$ the dynamic viscosity; details of parameter values can be found in Table 1.

We then introduce the following scalings:

$$x_\mathrm{f} = \frac{\tilde{x}}{\tilde{L}},\ y_\mathrm{f} = \frac{\tilde{y}}{\tilde{H}},\ Z_\mathrm{f} = \frac{\tilde{Z}}{\tilde{L}},\ v_x = \frac{\tilde{v}_x}{\tilde{V}},\ v_y = \frac{\tilde{v}_y}{\tilde{V}},\ v_Z = \frac{\tilde{v}_Z}{\tilde{V}},\ \text{and } t_\mathrm{f} = \frac{\tilde{V}}{\tilde{L}}\tilde{t}, \quad (1)$$

where the subscript 'f' refers to 'flow'. Note that variables with a tilde are dimensional and variables without a tilde are dimensionless. Making these substitutions into the Navier–Stokes equations, we find that to leading order in Re, the pressure is independent of y_f and $v_y = 0$ so that the flow occurs only in the x_f- and Z_f-directions.

The velocity profile is given by

$$v_x = y_\mathrm{f}(1 - y_\mathrm{f})F_x(x_\mathrm{f}, Z_\mathrm{f}), \quad v_Z = y_\mathrm{f}(1 - y_\mathrm{f})F_Z(x_\mathrm{f}, Z_\mathrm{f}). \quad (2)$$

Here F_x and F_Z are related to the pressure gradient and satisfy the constraint $\partial F_x/\partial Z_\mathrm{f} = \partial F_Z/\partial x_\mathrm{f}$. Formally, we also need to satisfy the no-slip condition at the channel walls $Z_\mathrm{f} = 0$ and $Z_\mathrm{f} = 1$. However, Edwards (2011) considers a boundary layer at the channel wall and shows that wall effects are minimal since the distance from the channel wall to the reacting zones is large compared to the thickness of the boundary layer; therefore, we neglect this additional complexity.

Table 1 Obtained and calculated parameter values for an optical biosensor

Parameter	Value	References
$\tilde{C}_u$ (mol/cm^3)	$2.96 \times 10^{-12} - 2 \times 10^{-10}$	Rich et al. (2008)
Da	$1.11 \times 10^{-6} - 7.64$	
$\tilde{D}$ (cm^2/s)	6.94×10^{-6}	Rich et al. (2008)
$\tilde{H}$ (cm)	0.018	GE Healthcare (2006)
K	$5 \times 10^{-5} - 3.38 \times 10^{4}$	
$\tilde{k}_{off}$ (1/s)	$10^{-5} - 10^{-2}$	GE Healthcare (2006)
$\tilde{k}_{on}$ (cm^3/mol s)	$10^{5} - 10^{9}$	GE Healthcare (2006)
$\tilde{L}$ (cm)	2.7	Rich et al. (2008)
$\tilde{L}_r$ (cm)	$1.5 \times 10^{-2} - 3.5 \times 10^{-2}$	GE Healthcare (2006)
Pe	$4.94 \times 10^{2} - 1.73 \times 10^{4}$	
$\tilde{R}$ (mol/cm^2)	$1.11 \times 10^{-13} - 2.33 \times 10^{-11}$	Rich et al. (2008)
Re	≤ 0.067	
$\tilde{V}$ (cm/s)	$3.70 \times 10^{-1} - 5.56$	
$\tilde{W}$ (cm)	1.5	Rich et al. (2008)

2.2 Injection phase model

Given the velocity profile from the previous section, we may now consider the evolution of the ligand concentration $\tilde{C}$, which in dimensional variables follows the standard convection-diffusion equation

$$\frac{\partial \tilde{C}}{\partial \tilde{t}} = \nabla^2 \tilde{C} - \tilde{\mathbf{v}} \cdot \nabla \tilde{C}. \tag{3}$$

Given the aspect ratios described in Sect. 2.1, we see that diffusion in the $\tilde{y}$-direction dominates. Moreover, by Eq. (2), we see that this term must balance with convection in the $\tilde{x}$- and $\tilde{Z}$-directions.

However, for biosensor experiments, the velocity within the device is large compared to the diffusion constant so that the rate of convection to the rate of diffusion given by the Peclét number $\mathrm{Pe} = \tilde{V}\tilde{H}^2/\tilde{D}\tilde{L}_r$ is large. Therefore, ligand molecules in the bulk will flow out of the cell before they have time to diffuse to the reacting surface. Hence we focus our attention on a thin boundary layer near the reacting surface $\tilde{y} = 0$ by letting $\eta = \mathrm{Pe}^{1/3} y_f$.

To simplify our analysis, we introduce the new scaled variables

$$\tilde{C}(\tilde{x}, \tilde{y}, \tilde{Z}, \tilde{t}) = \tilde{C}_u(1 - C(x, y, Z, t)),\ x = \frac{\tilde{x}}{\tilde{L}_r},\ Z = \frac{\tilde{Z}}{\tilde{L}_r},\ t = \frac{1}{\tilde{C}_u \tilde{k}_{on}} \tilde{t}, \tag{4}$$

where $\tilde{L}_r$ is the length of a reacting zone, $\tilde{C}_u$ the uniform feed concentration, and $\tilde{k}_{on}$ the association rate constant. When we derived the flow expression in the previous

section, we used the variables x_f and Z_f, which were scaled by the dimensions of the flow cell. Now that we are interested in the reaction kinetics, we introduce the variables x and Z, which are scaled by the dimensions of the reacting zone. Note also the scaling of the ligand concentration; we expect minimal change from the feed concentration and scale C to represent the dimensionless ligand depletion from the uniform feed concentration. Finally, we note that time has been scaled by the forward reaction time scale.

Substituting Eq. (4) into Eq. (3), we obtain

$$\frac{\partial^2 C}{\partial \eta^2} = \eta\left(F_x \frac{\partial C}{\partial x} + F_Z \frac{\partial C}{\partial Z}\right), \tag{5}$$

where we have used Eq. (2). This equation is analogous to equation (3.3) in the one-dimensional system by Edwards (2011); the only change is the inclusion of both F_x and F_Z in Eq. (5). Note that in the two-dimensional system, η plays the role of a parameter that can be factored from each term in the right-hand side of Eq. (5).

Note that t no longer appears in Eq. (5), because we have chosen to use the reaction time scale, which in experiments is much longer than the diffusive time scale. Hence the diffusive transport is in steady state, and the ligand concentration changes only due to binding at the reacting surface.

We denote the dimensional bound state by $\tilde{B}$; then by introducing

$$B(x, Z, t) = \frac{\tilde{B}(\tilde{x}, \tilde{Z}, \tilde{t})}{\tilde{R}}, \tag{6}$$

where $\tilde{R}$ is the uniform receptor concentration, the governing reversible kinetics equation is given by

$$\frac{\partial B}{\partial t} = (1 - B)(1 - C(x, 0, Z, t)) - KB. \tag{7}$$

Here $K = \tilde{k}_\mathrm{off}/\tilde{C}_\mathrm{u}\tilde{k}_\mathrm{on}$ is a scaled affinity constant, where $\tilde{k}_\mathrm{off}$ is the dissociation rate constant.

Equations (5) and (7) must then be solved subject to

$$C(0, \eta, Z, t) = 0, \tag{8}$$

$$\frac{\partial C}{\partial \eta}(x, 0, Z, t) = -\mathrm{Da}\frac{\partial B}{\partial t}, \qquad \mathrm{Da} = \frac{k_\mathrm{on} R}{D/(H\mathrm{Pe}^{-1/3})}, \tag{9}$$

$$B(x, Z, 0) = 0, \tag{10}$$

$$C(x, \infty, Z, t) = 0. \tag{11}$$

Summarizing, Eq. (8) is the ligand depletion from the uniform concentration $\tilde{C}_\mathrm{u}$ at the flow inlet, Eq. (9) the diffusive flux at the reacting surface creating bound receptors, Eq. (10) the initial condition for bound receptors, and Eq. (11) the boundary layer ligand concentration far-field condition matching the uniform ligand concentration in the bulk. In Eq. (9), the Damköhler number Da is the ratio of the rate of reaction to the rate of diffusion.

We limit ourselves to the experimental regime $\mathrm{Da} \ll 1$, corresponding to the reaction-limited problem. With $\mathrm{Da} = 0$ in Eqs. (5), (8), (9), and (11), we find that $C = 0$, so there is no leading-order ligand depletion. With this result and a perturbation expansion for the bound state

$$B(x, Z, t) = B_0(x, Z, t) + \mathcal{O}(\mathrm{Da}), \tag{12}$$

the leading-order bound state is

$$B_0(t) = \frac{1 - e^{-(1+K)t}}{1 + K}. \tag{13}$$

Since the amount of ligand used in reactions is small enough to be neglected at leading order, we scale the ligand depletion C by letting $C = \mathrm{Da}C_1$ in Eqs. (5), (8), (9), and (11) to obtain the following system for ligand depletion:

$$\frac{\partial^2 C_1}{\partial \eta^2} = \eta\left(F_x \frac{\partial C_1}{\partial x} + F_Z \frac{\partial C_1}{\partial Z}\right), \tag{14}$$

$$C_1(0, \eta, Z, t) = 0, \tag{15}$$

$$\frac{\partial C_1}{\partial \eta}(x, 0, Z, t) = -\frac{\partial B}{\partial t}, \tag{16}$$

$$C_1(x, \infty, Z, t) = 0. \tag{17}$$

To examine ligand depletion along streamlines for two-dimensional flow, we convert to a coordinate system in terms of ξ and γ, where γ is constant along streamlines and streamlines are trajectories of the velocity field

$$\frac{\partial x}{\partial \xi} = F_x, \quad \frac{\partial Z}{\partial \xi} = F_Z. \tag{18}$$

Figure 2 shows a sample streamline with the (ξ, γ) coordinate system in the xZ-plane. This conversion is useful since the directional derivative

$$\begin{aligned} F_x \frac{\partial C_1}{\partial x} + F_Z \frac{\partial C_1}{\partial Z} &= \frac{\partial C_1}{\partial x}\frac{\partial x}{\partial \xi} + \frac{\partial C_1}{\partial Z}\frac{\partial Z}{\partial \xi} \\ &= \frac{\partial C_1}{\partial \xi} \end{aligned}$$

is in the ξ-direction.

In the (ξ, η, γ) coordinate system, Eqs. (14)–(17) simplify to

$$\frac{\partial^2 C_1}{\partial \eta^2} = \eta \frac{\partial C_1}{\partial \xi}, \tag{19}$$

$$C_1(0, \eta, \gamma, t) = 0, \tag{20}$$

$$\frac{\partial C_1}{\partial \eta}(\xi, 0, \gamma, t) = -\frac{\partial B}{\partial t}, \tag{21}$$

$$C_1(\xi, \infty, \gamma, t) = 0, \tag{22}$$

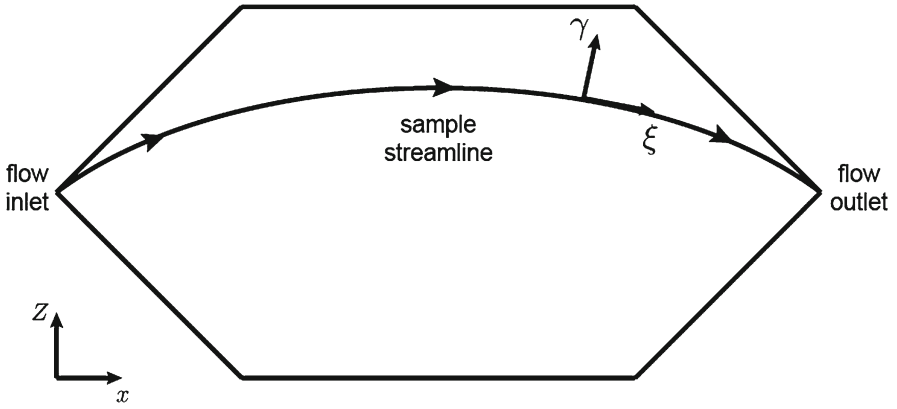

Fig. 2 Representation of the (ξ, γ) coordinate system along a sample streamline in the xZ-plane

which is exactly the system for unidirectional flow since flow in the (ξ, η, γ) coordinate system occurs in the ξ-direction. Using the Laplace transform in ξ, Eqs. (19) and (20) become Airy's equation for $\widehat{C}_1$, the Laplace transform of C_1. Solving this equation subject to the transformed versions of Eqs. (21) and (22), we have

$$\widehat{C}_1(s, \eta, t) = -\frac{d\widehat{B}}{dt}\frac{\mathrm{Ai}(s^{1/3}\eta)}{\mathrm{Ai}'(0)s^{1/3}},$$

where $\widehat{B}$ is the Laplace transform of B and s the transformed variable.

We need only the value at $\eta = 0$; using the convolution theorem we have that the $\mathcal{O}(\mathrm{Da})$ ligand depletion measured along streamlines is given by

$$\begin{aligned} C_1(\xi, 0, t; \gamma) &= \frac{1}{3^{1/3}\Gamma(2/3)}\int_0^{\xi}\frac{\partial B}{\partial t}(\nu, \gamma, t)(\xi - \nu)^{-2/3}\,d\nu \\ &= \frac{dB_0}{dt}h(\xi; \gamma) + \mathcal{O}(\mathrm{Da}), \quad h(\xi; \gamma) = \frac{3^{2/3}}{\Gamma(2/3)}\xi^{1/3}. \end{aligned} \tag{23}$$

With the perturbation expansion given in Eq. (12), the derivative of the spatially-uniform leading-order bound state can be factored from the integral. While γ is not included explicitly in this expression, it identifies the specific streamline for integration, affecting the ligand depletion quantity.

3 Schwarz–Christoffel mapping

The Schwarz–Christoffel (SC) mapping for the infinite strip to a polygon is

$$f(z) = A + S\int^{z}\prod_{k=1}^{n}\left(\sinh\frac{\pi}{2}(\zeta - z_k)\right)^{\alpha_k - 1}d\zeta,$$

where A is the unknown location parameter, S the unknown scaling parameter, n the number of vertices exclusive of the strip ends, z_k the unknown prevertices, and $\alpha_k\pi$ the interior angles at the mapped vertices in the polygon (Driscoll and Trefethen 2002). The mapping is similar to that for the half-plane to a polygon, except for the sinh function which is necessary due to the additional upper boundary Im $z = 1$ for the strip. The SC mapping from the half-plane to the polygon is defined so that the derivative, the product of the functions $(z - z_k)^{\alpha_k - 1}$, has piecewise constant argument when mapping the real axis to the boundary of the polygon; the only jumps in the argument occur at the prevertices z_k. For the mapping of the strip to the polygon, the derivative cannot include only the simple functions $(z - z_k)^{\alpha_k - 1}$. For a real prevertex and any z on the upper boundary of the strip, the argument of each of these functions changes as z moves along the boundary; hence the product does not have piecewise constant argument. Therefore, the sinh function is necessary for mapping the upper boundary of the strip to a radial slit of constant argument, while still mapping the real axis to itself.

3.1 General trapezoid mappings

Exploiting the symmetry of the device in the Z-direction, we map the infinite strip to the lower half of the Flexchip hexagon and extend results to the upper half. For a Flexchip of length $\tilde{L}$ and width $\tilde{W}$, the trapezoid has length $\tilde{L}$, width $\tilde{W}/2$, and acute angle $\theta\pi$, and we specify the following five mappings from the strip to the trapezoid, represented in Fig. 3:

$$\begin{aligned} f(-z_1) &= -\frac{\tilde{L}}{2} + \frac{\tilde{W}}{2}\cot\theta\pi, \quad \text{(dotted circle)} \\ f(0) &= 0, \quad \text{(empty circle)} \\ f(z_1) &= \frac{\tilde{L}}{2} - \frac{\tilde{W}}{2}\cot\theta\pi, \quad \text{(filled circle)} \\ f(-\infty) &= -\frac{\tilde{L}}{2} + \frac{\tilde{W}}{2}i, \qquad f(\infty) = \frac{\tilde{L}}{2} + \frac{\tilde{W}}{2}i. \end{aligned} \tag{24}$$

In these mappings, we have also exploited the horizontal symmetry to write the prevertices as $\pm z_1$ instead of unrelated prevertices z_1, z_2. Generally, the upper boundary of the strip is mapped to the longer trapezoid base while the lower boundary of the strip is mapped to the other three sides.

Since the acute angle in the trapezoid is $\theta\pi$, the interior angle at the mapped vertices corresponding to the prevertices $z = \pm z_1$ is $(1-\theta)\pi$ so that $\alpha = 1-\theta$. For the mapping of the origin, the interior angle is π so that $\alpha = 1$; therefore, the exponent for the corresponding term in the SC mapping is zero, and we omit this term. The mapping from the strip to the trapezoid is

$$f(z) = A + S\int^z \left(\sinh\frac{\pi}{2}(\zeta + z_1)\sinh\frac{\pi}{2}(\zeta - z_1)\right)^{(1-\theta)-1} d\zeta. \tag{25}$$

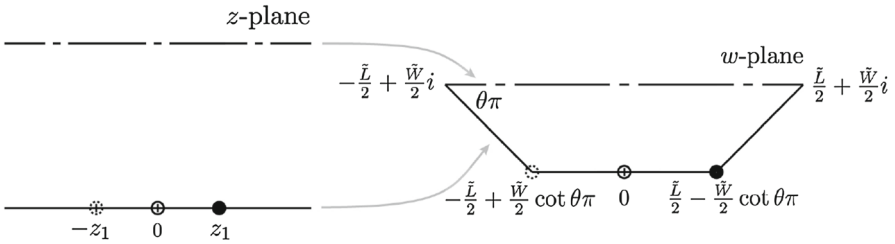

Fig. 3 Representation of vertex mappings from the strip to the trapezoid. The same symbols are used for vertex-prevertex pairs. Note that the upper corners of the trapezoid are mapped from the corresponding strip ends

The lower bound of the integral is left unspecified, and we take this to be zero without loss of generality. From the mapping of the origin, we have $0 = f(0) = A$; therefore, Eq. (25) is defined in terms of the unknowns S and z_1. To obtain two equations in terms of these parameters, we use the four remaining mappings. As a result of the horizontal symmetry, we obtain one equation from the mapping of the prevertices $f(\pm z_1)$ and a second equation from the mapping of the strip ends $f(\pm\infty)$.

From the mapping for $f(z_1)$, we have

$$\begin{aligned}\frac{\tilde{L}}{2}-\frac{\tilde{W}}{2}\cot\theta\pi &= f(z_1)\\ &= S\int_0^{z_1}\left(\sinh\frac{\pi}{2}(\zeta+z_1)\sinh\frac{\pi}{2}(\zeta-z_1)\right)^{-\theta}d\zeta\\ &= D\int_0^{z_1}\left(\sinh\frac{\pi}{2}(\zeta+z_1)\sinh\frac{\pi}{2}(z_1-\zeta)\right)^{-\theta}d\zeta, \qquad (26)\end{aligned}$$

where $D = Se^{-i\pi\theta}$ is real since the left-hand side and the integral in the right-hand side of Eq. (26) are real. Manipulation of the mapping for $f(-z_1)$ also yields this equation.

From the mapping $f(\infty)$ at the strip end, we have

$$\begin{aligned}\frac{\tilde{L}}{2}+\frac{\tilde{W}}{2}i &= f(\infty)\\ &= S\int_0^{\infty}\left(\sinh\frac{\pi}{2}(\zeta+z_1)\sinh\frac{\pi}{2}(\zeta-z_1)\right)^{-\theta}d\zeta\\ &= S\int_0^{z_1}\left(\sinh\frac{\pi}{2}(\zeta+z_1)\sinh\frac{\pi}{2}(\zeta-z_1)\right)^{-\theta}d\zeta\\ &\quad +S\int_{z_1}^{\infty}\left(\sinh\frac{\pi}{2}(\zeta+z_1)\sinh\frac{\pi}{2}(\zeta-z_1)\right)^{-\theta}d\zeta.\end{aligned}$$

Recognizing that the first integral is simply $f(z_1)$, we make this substitution and obtain

$$\frac{\tilde{W}}{2}\cot\theta\pi+\frac{\tilde{W}}{2}i = De^{i\pi\theta}\int_{z_1}^{\infty}\left(\sinh\frac{\pi}{2}(\zeta+z_1)\sinh\frac{\pi}{2}(\zeta-z_1)\right)^{-\theta}d\zeta.$$

Using $e^{i\pi\theta} = \sin\theta\pi(\cot\theta\pi + i)$, we have

$$\frac{\tilde{W}}{2} = D\sin\theta\pi \int_{z_1}^{\infty} \left(\sinh\frac{\pi}{2}(\zeta + z_1)\sinh\frac{\pi}{2}(\zeta - z_1)\right)^{-\theta} d\zeta \tag{27}$$

and obtain the same equation from the mapping $f(-\infty)$.

Solving for D in terms of z_1 in Eq. (26), we have

$$D = \frac{\tilde{L} - \tilde{W}\cot\theta\pi}{2\displaystyle\int_0^{z_1} \left(\sinh\frac{\pi}{2}(\zeta + z_1)\sinh\frac{\pi}{2}(z_1 - \zeta)\right)^{-\theta} d\zeta}; \tag{28}$$

substituting Eq. (28) in Eq. (27), we obtain the equation

$$g\left(z_1; \theta, \frac{\tilde{L}}{\tilde{W}}\right) = \left(\frac{\tilde{L}}{\tilde{W}} - \cot\theta\pi\right)\sin\theta\pi \times \frac{\displaystyle\int_{z_1}^{\infty} \left(\sinh\frac{\pi}{2}(\zeta + z_1)\sinh\frac{\pi}{2}(\zeta - z_1)\right)^{-\theta} d\zeta}{\displaystyle\int_0^{z_1} \left(\sinh\frac{\pi}{2}(\zeta + z_1)\sinh\frac{\pi}{2}(z_1 - \zeta)\right)^{-\theta} d\zeta} - 1 = 0, \tag{29}$$

where the value of the prevertex z_1 depends on the aspect ratio $\tilde{L}/\tilde{W}$ and interior angle $\theta\pi$ of the trapezoid. For simplicity, we use the method of bisections to calculate z_1. For the problems under consideration, this takes approximately 35 iterations and 3 seconds of CPU time to calculate z_1 with an error tolerance of 10^{-10}. With a value for z_1, we calculate D from Eq. (28).

3.2 Flexchip mapping examples

Unable to obtain exact dimensions of the actual Flexchip device, we include several possible sets of dimensions and corresponding mappings. Information from two sources is used to develop four possible sets of dimensions of the actual device. In each case, we include the calculated parameters D and z_1 in Table 2 at the end of the section. We also include parameter values generated using the SC Toolbox for MATLAB, a software package that allows users to easily produce conformal maps from both bounded and unbounded domains, such as polygons, disks, and strips, to polygons. Additional details can be found in Driscoll (2013).

In Rich et al. (2008), Figure 1A displays a picture of a Flexchip flow cell, and we scale the measured dimensions using the labeled 1-cm square array to calculate the physical dimensions. The calculated length $\tilde{L}$ and width $\tilde{W}$ are 2.7 and 1.5 cm respectively, so that the area of the hexagon is 315 mm^2. Using the symmetry of the device, we calculate the measure of the acute angle as 51°. As this measure is $\theta\pi$ radians, we have that $\theta = 0.28522$. We display the corresponding streamline mapping generated by the SC Toolbox in Fig. 4. Note that the prevertices are shifted horizontally

Table 2 Parameters D and z_1 calculated from Eqs. (28) and (29) or obtained from SC Toolbox

	Calculated		SC Toolbox	
	D	z_1	D	z_1
Measured dimensions from Fig 1A in Rich et al. (2008)				
Raw[a]	1.04209	0.808902	1.04209	0.808902
Scaled	0.938628	0.808902	0.938626	0.808903
Simulation parameters in Rich et al. (2008)				
Raw	0.910743	0.755438	0.910743	0.755438
Scaled	0.994088	0.755438	0.994088	0.755436

[a] Used in Sect. 4

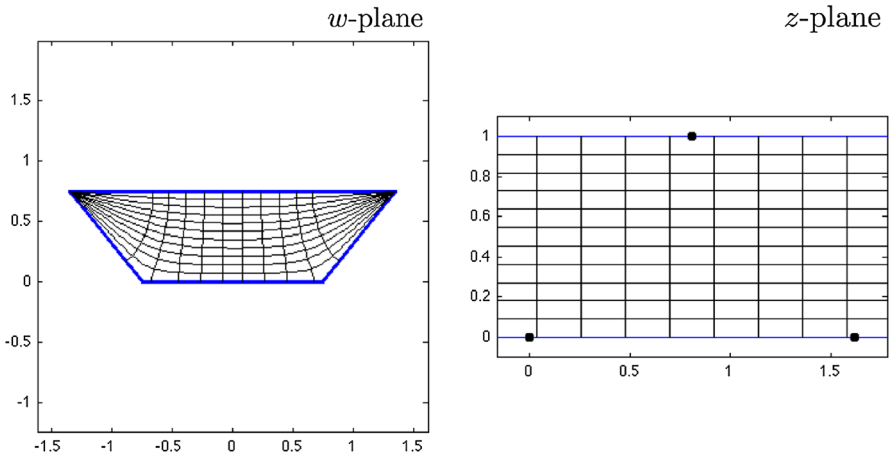

Fig. 4 Mapping of the Flexchip using measured dimensions in Rich et al. (2008)

from the values we obtain due to a different choice for the lower bound of the mapping. We produce another mapping using the numerical simulation dimensions given in Rich et al. (2008). The length $\tilde{L}$ and width $\tilde{W}$ are 2 and 1.3 cm respectively, so that the area of the hexagon is 214.5 mm^2. Using the symmetry of the device again, we calculate the measure of the acute angle as 62°, which corresponds to $\theta = 0.34277$.

General Electric (GE) production specifications identify the Flexchip flow cell volume and flow cell height as 46 and 180 μm respectively (GE Healthcare 2006), so that the flow cell area is approximately 255 mm^2. To achieve the area specified by GE, we scale the length and width to produce an additional mapping for each of the previous cases.

For the measured data, we scale the dimensions by the square root of the ratio of the GE-specified area to the calculated area to obtain $\tilde{L} \approx 2.43$ cm and $\tilde{W} \approx 1.35$ cm for the corresponding θ. Similarly, we scale the simulation dimensions to obtain $\tilde{L} \approx 2.18$ cm and $\tilde{W} \approx 1.42$ cm for the corresponding θ.

Note that D is simply the value from the raw dimensions scaled by the area ratio so that the area is changed to match the GE specifications. The value for z_1 is unaffected

by the scaling since z_1 depends only on the aspect ratio and the interior angle, and all changes due to scaling are accounted for with the parameter D. In both scaled cases, the dimensions of the scaled trapezoids with area equal to the GE specifications are within 10 % of the dimensions of the original trapezoids. For each mapping, flow over the centered unit square where reacting zones are located is approximately unidirectional (see Fig. 4 or the CDF simulation in Rich et al. (2008)), making the assumption of unidirectional flow reasonable.

In the calculation of parameter values and analysis that follows, we use the trapezoid dimensions obtained from the device pictured in Rich et al. (2008) and mapped in Fig. 4, since the cited figure provides more detail and additional reliability than the unreferenced dimensions used in the numerical simulation. We do not account for the difference in the hexagon area for the measured dimensions and GE specifications since there may be subtleties in the definition of flow cell volume of which we are not aware.

4 Flexchip ligand concentration comparison

For a general conformal mapping $f(z)$, if $f'(z_0) \neq 0$ for the point z_0, the transformation not only rotates all line segments through z_0 by the same angle but also stretches all line segments through z_0 by the factor $|f'(z_0)|$ (Carrier et al. 2005). For ξ in the trapezoid, we have $d\xi = |f'(z)|\,dz$ for z in the strip so that $\xi = \int |f'(z)|\,dz$. Therefore, using the SC mapping and assuming the that the entire surface of the trapezoid is a reacting zone, we can find ξ along streamlines in the trapezoid from streamlines in the strip using

$$\xi = \int_{-\infty}^{\alpha} |f'(x + \beta i)|\,dx, \tag{30}$$

where $f(\alpha + \beta i) = w^*$ is the terminal point of the contour in the trapezoid. In Fig. 5, we display a sample streamline in the trapezoid with terminal point w^* and the corresponding streamline in the strip with constant β.

To quantify the maximum ligand depletion ratio between points mapped from a constant α throughout a device, we compare the maximum and minimum values of Eq. (30) for varying β by considering

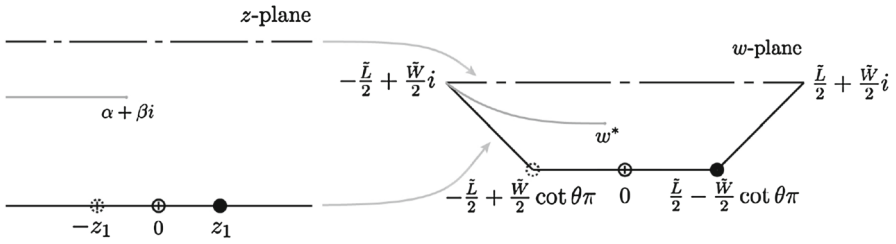

Fig. 5 Representation of a streamline in the trapezoid with terminal point w^* and the corresponding streamline in the strip with constant β

$$\frac{\partial}{\partial\beta}\int_{-\infty}^{\alpha}|f'(x+\beta i)|\,dx. \tag{31}$$

For simplicity, we neglect the cube root in Eq. (23) since extrema of Eq. (31) are also extrema of Eq. (23).

We first obtain a simpler expression for $f'(x+\beta i)$ in Eq. (31) by writing the SC mapping in terms of cosh functions, specifically

$$f(z) = 2^{\theta} S\int_{0}^{z}(\cosh\pi\zeta - \cosh\pi z_1)^{-\theta}d\zeta.$$

Letting $z = x+\beta i$, we compute the derivative

$$\begin{aligned} f'(x+\beta i) &= 2^{\theta} S(\cosh\pi(x+\beta i) - \cosh\pi z_1)^{-\theta} \\ &= 2^{\theta} S(\cosh\pi x\cos\pi\beta - \cosh\pi z_1 + i\sinh\pi x\sin\pi\beta)^{-\theta}. \end{aligned}$$

Differentiating the modulus of this expression, we obtain the partial derivative of the integrand of Eq. (31) with

$$\begin{aligned} \frac{\partial}{\partial\beta}|f'(x+\beta i)| = &-\left((\cosh\pi x\cos\pi\beta - \cosh\pi z_1)^2 + \sinh^2\pi x\sin^2\pi\beta\right)^{-\theta/2-1} \\ &\times 2^{\theta}|S|\theta\pi(\cosh\pi z_1\cosh\pi x - \cos\pi\beta)\sin\pi\beta. \end{aligned} \tag{32}$$

To determine the sign of the right-hand side of Eq. (32), we examine the sign of individual terms of this expression. The $\cosh\pi z_1\cosh\pi x - \cos\pi\beta$ and $\sin\pi\beta$ terms are nonnegative for $0 \le \beta \le 1$. The fact that the $\cosh\pi z_1\cosh\pi x - \cos\pi\beta$ term is positive is subtle, but the smallest this term can be is zero, which only occurs if $\beta = 0$, $z_1 = 0$, and $x = 0$. However, $z_1 = 0$ is not a physically relevant case since the polygon produced in this case is a triangle, not a trapezoid. The $(\cosh\pi x\cos\pi\beta - \cosh\pi z_1)^2 + \sinh^2\pi x\sin^2\pi\beta$ term is nonnegative and zero for two cases. The first case occurs if $x = 0$ and $\cos\pi\beta = \cosh\pi z_1$, possible only if $z_1 = 0$. The second case occurs if $\beta = 0$ and $\cosh\pi x = \cosh\pi z_1$ with $x = \pm z_1$; hence, the integrand is not differentiable at the prevertices. Therefore, where it is defined, the right-hand side of Eq. (32) is always negative, and depletion decreases as β increases. Therefore, for points mapped from the same α, the ligand concentration is largest for $\beta = 1$ and smallest at $\beta = 0$, corresponding to the center line and wall of the device respectively as represented in Fig. 3. In Fig. 6, we display the graph of the right-hand side of Eq. (32) for the trapezoid using measured data with various β. We see the behavior of the derivative near the prevertices $\pm z_1 = 0.808902$ is exactly as we expect as β decreases.

We find the dimensional ligand concentration using the $\mathcal{O}(\mathrm{Da})$ depletion from the uniform feed concentration given in Eq. (23) and compute the maximum ligand concentration ratio for varying β with a constant α, which is the ratio of the ligand

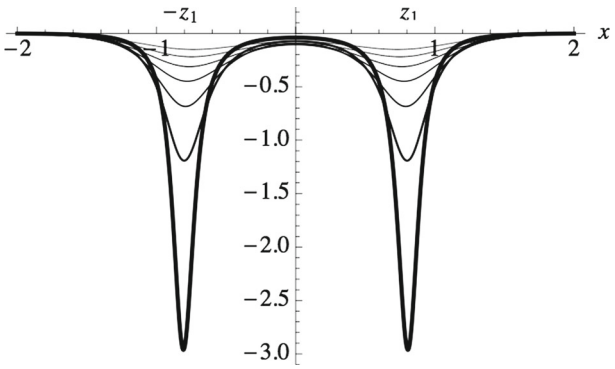

Fig. 6 Derivative represented by the right-hand side of Eq. (32) for the measured trapezoid example with $\beta = 0.1, 0.2, 0.3, \ldots, 0.7$ (decreasing thickness)

concentration for $\beta = 1$ to the ligand concentration for $\beta = 0$:

$$r(t;\alpha) = \frac{\tilde{C}_{\mathrm{u}}\left(1 - \mathrm{Da}\frac{3^{2/3}}{\Gamma(2/3)}\frac{dB_0}{dt}\xi_{\beta=1}^{1/3}\right)}{\tilde{C}_{\mathrm{u}}\left(1 - \mathrm{Da}\frac{3^{2/3}}{\Gamma(2/3)}\frac{dB_0}{dt}\xi_{\beta=0}^{1/3}\right)}. \tag{33}$$

Because $\xi_{\beta=0} > \xi_{\beta=1}$, $r(t;\alpha)$ is a decreasing function of t and is maximized for $t = 0$ when $dB_0/dt = 1$. Therefore, we have the bound for Eq. (33) in terms of the parameter α

$$r(t;\alpha) \le r(0;\alpha) = \frac{1 - \mathrm{Da}\frac{3^{2/3}}{\Gamma(2/3)}\xi_{\beta=1}^{1/3}}{1 - \mathrm{Da}\frac{3^{2/3}}{\Gamma(2/3)}\xi_{\beta=0}^{1/3}}, \tag{34}$$

where

$$\xi_{\beta=1}^{1/3} = \left(f(\alpha + i) - f(-\infty)\right)^{1/3}$$

and

$$\xi_{\beta=0}^{1/3} = \begin{cases} (e^{i\theta\pi}(f(\alpha) - f(-\infty)))^{1/3}, & \alpha \le -z_1 \\ (e^{i\theta\pi}(f(-z_1) - f(-\infty)) + f(\alpha) - f(-z_1))^{1/3}, & -z_1 \le \alpha \le z_1 \\ (e^{i\theta\pi}(f(-z_1) - f(-\infty)) + 2f(z_1) + e^{-i\theta\pi}(f(\alpha) - f(z_1)))^{1/3}, & \alpha \ge z_1 \end{cases}$$

for a general angle $\theta\pi$. Using the parameters calculated in Sect. 3.2 for the trapezoid dimension measured from Figure 1A in Rich et al. (2008), we display the graph of the right-hand side of Eq. (34) in Fig. 7 with $\mathrm{Da} = 0.1$. The graph has quick changes in the function values near the prevertices $\pm z_1 = \pm 0.808902$, which can be attributed to the derivative including a factor of $f'(\alpha)$. Since $f'(\alpha)$ is undefined at the prevertices $\pm z_1$ for $\beta = 0$, the function values change quickly near these points. Physically, these points correspond to turning the corner at the obtuse angle along the wall of the trapezoid.

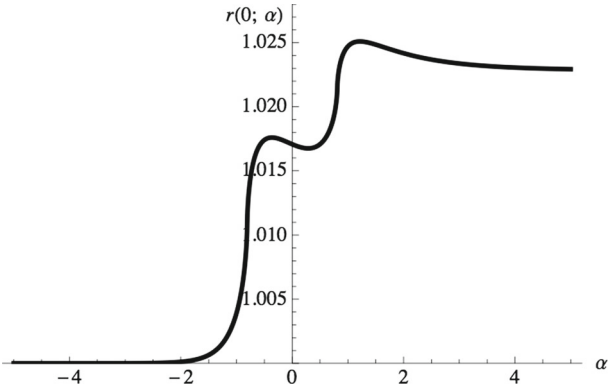

Fig. 7 $r(0;\alpha)$ (as given by the right-hand side of Eq. (34)) vs. α for Da $= 0.1$. Here r is the ratio of the depleted ligand concentration at the exterior wall of the Flexchip to a unidirectional channel; $r(0;\alpha)$ is the upper bound on r

We see that the ligand concentration disparity between points mapped from the same α along the center line and the wall of the Flexchip is less than 3 % for Da $= 0.1$. Since we have maximized this ratio with respect to time, this disparity decreases as an experiment proceeds. Since this ratio is directly related to the Damköhler number, physical parameters resulting in a larger Damköhler number produce a larger concentration disparity in the device. In this calculation, we have not accounted for an array of reacting zones, and the array configuration might further complicate ligand depletion within a device.

5 Estimation of rate constants

Experimentalists often run a biological assay to obtain rate constants for a specific interaction. To calculate these constants, a biosensor produces a sensogram, the spatial average of the bound ligand concentration over a reacting zone as a function of time. For a reacting zone $\mathcal{R}$ with area A, we define the sensogram

$$S[B](t) = \frac{1}{A}\iint_{\mathcal{R}} B\, dA.$$

To obtain a sensogram expression, we average Eq. (7), and use the perturbation expansion for the bound ligand concentration in Eq. (12) and the $\mathcal{O}(\mathrm{Da})$ ligand concentration in Eq. (23); details can be found in (Zumbrum 2014).

We use the dimensional sensogram expression

$$S[B](\tilde{t}) = \frac{\tilde{C}_u\tilde{k}_{on}(1 - e^{-(\tilde{C}_u\tilde{k}_{on}+(1-\mathrm{Da}S[h])\tilde{k}_{off})\tilde{t}})}{\tilde{C}_u\tilde{k}_{on} + \tilde{k}_{off} + \tilde{C}_u\tilde{k}_{on}\frac{\mathrm{Da}S[h]}{1-\mathrm{Da}S[h]}e^{-(\tilde{C}_u\tilde{k}_{on}+(1-\mathrm{Da}S[h])\tilde{k}_{off})\tilde{t}}} \tag{35}$$

to include the rate constants $\tilde{k}_{on}$ and $\tilde{k}_{off}$ for association and dissociation respectively. In Eq. (35), depletion effects are accounted for in the $S[h]$ term. For two-dimensional

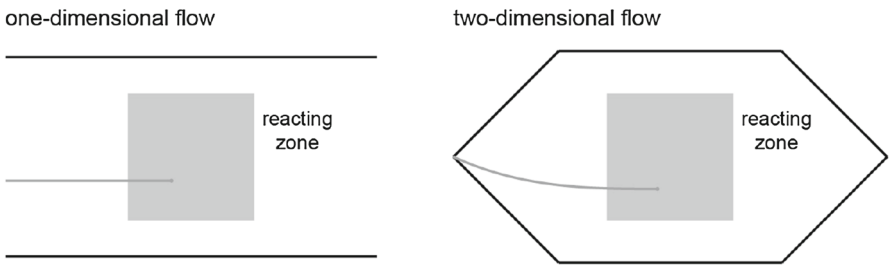

Fig. 8 Representation of a unit square reacting zone in a channel with one-dimensional flow and in the Flexchip with two-dimensional flow

flow, $S[h]$ is the average of $h(\xi;\gamma)$ from Eq. (23). Note that for a unit square reacting zone centered in the Flexchip, we redefine

$$\xi = \int_0^{\alpha} |f'(x+\beta i)|\,dx + 0.5$$

from Eq. (30) so that along the centerline of the trapezoid, the reacting zone begins at $\xi = 0$ and ends at $\xi = 1$. For one-dimensional flow over a unit square reacting zone, $S[h] = 1.15209$ (Zumbrum 2014); for two-dimensional flow over the same reacting zone centered in the Flexchip, $S[h] = 1.17276$ and the increase in this parameter is due to increased ligand depletion for two-dimensional flow. Figure 8 displays a schematic representation of one-dimensional and two-dimensional flow over a unit square reacting zone. Using rate constants in the ranges

$$\tilde{k}_{\text{on}} = 10^5 - 10^8\,\text{cm}^3/\text{mol}\,\text{s} \text{ and } \tilde{k}_{\text{off}} = 10^{-5} - 10^{-2}\,\text{s}^{-1} \tag{36}$$

and assuming a uniform feed concentration $\tilde{C}_{\text{u}} = 10^{-11}\,\text{mol/cm}^3$, we calculate sensograms $S[B](\tilde{t})$ from Eq. (35) with $\tilde{t} \in [0, 35000]$ seconds and sample at integer times to obtain simulated sensogram data.

To determine how ignoring two-dimensional flow distorts the measurement of rate constants, we fit Eq. (35) for one-dimensional flow to the simulated sensogram data for two-dimensional flow using the least-squares fitting command `FindFit` in Mathematica. In other words, we naïvely assume one-dimensional flow over the reacting zone. Since the simulated data includes additional depletion effects due to two-dimensional flow, we expect to obtain estimates for the rate constants that are smaller than the exact values.

We consider various rate constant combinations for specific Damköhler numbers and compute estimated rate constants for each, which are displayed in Table 3.
We increase Da with $\tilde{k}_{\text{on}}$ to keep all other parameters in Eq. (9) constant. We see that the relative error for the estimated rate constants increases for larger association rates. This can be attributed to the fact that depletion along streamlines in two-dimensional flow increases for larger association rates and larger Damköhler numbers; neglecting this additional depletion using the one-dimensional model makes this effect more pronounced. However, the relative error for even the worst case is only 2 %, and naïve use of the one-dimensional model produces reasonable results. Note that the relative

Table 3 Estimated rate constants for a reacting zone using the naïve one-dimensional model

	$\tilde{k}_{on}$ ($cm^3/mol\,s$)		$\tilde{k}_{off}$ (s^{-1})	
	Exact	Estimate	Exact	Estimate
$Da = 10^{-4}$	10^6	9.99880×10^5	10^{-5}	9.99409×10^{-6}
$Da = 10^{-3}$	10^7	9.99754×10^6	10^{-4}	9.99724×10^{-5}
$Da = 10^{-2}$	10^8	9.97844×10^7	10^{-3}	9.97829×10^{-4}
$Da = 10^{-1}$	10^9	9.80361×10^8	10^{-2}	9.80347×10^{-3}

Despite additional ligand depletion, the one-dimensional model produces estimates for the rate constants with less than 2 % error

error in the estimated rate constants is directly related to Da; if experimentalists can decrease Da via other experimental parameters, such as using a higher flow velocity, estimates with smaller error can be obtained.

These results consider a reacting zone centered in the Flexchip. If the reacting zone were to be moved vertically off center, depletion over streamlines shorter than those included in previous results (see streamlines near the lower wall in the left-hand side of Fig. 4) would be included in the average depletion term; hence average depletion would decrease. If the reacting zone were to be moved horizontally off center, streamlines longer than those included in the previous results (see streamlines above the angles in the left-hand side of Fig. 4) would increase the average depletion term. In either case, we expect these effects to be minimal due to the small change in depletion over the streamlines.

6 Conclusion

Mathematical models for surface-volume reactions within optical biosensors have long utilized the assumption of unidirectional flow. This assumption is mathematically useful but not physically representative of the dynamics within some optical biosensors; therefore, we considered the physically-relevant case of two-dimensional flow.

Mapping the infinite strip to the physical domain using the Schwarz–Christoffel mapping allowed for the extension of results from the unidirectional flow case to the two-dimensional flow case for the Biacore Flexchip. We produced several mappings for possible device dimensions and used one of these mappings to quantify depletion throughout the device, assuming the entire device floor is a reacting surface.

To determine the effect of two-dimensional flow in the measurement of rate constants, we fit the model for one-dimensional flow to simulated data produced from the model for two-dimensional flow. For combinations of rate constants on varying orders of magnitude, the relative error of the estimated rate constants was less than 2 % in each case, meaning that ignoring two-dimensional flow in the model still produced reasonable results. These results should be helpful for experimentalists; the simpler one-dimensional model can be used instead of the more complicated two-dimensional model because the added complexity has a small effect.

The Schwarz–Christoffel mapping discussed could be used with previous results over arrays by Edwards (2011) to produce better models for average bound ligand concentration over a reacting zone within a rectangular array, and it would be particularly interesting to further investigate non-rectangular array layouts to minimize or simplify depletion effects.

References

Carrier GF, Krook M, Pearson CE (2005) Functions of a complex variable: theory and technique (classics in applied mathematics). Society for Industrial and Applied Mathematics, Philadelphia

Driscoll T, Trefethen L (2005) Schwarz–Christoffel mapping (Cambridge monographs on applied and computational mathematics). Cambridge University Press, Cambridge

Driscoll TA (2013) The Schwarz–Christoffel toolbox for MATLAB. http://www.math.udel.edu/~driscoll/SC

Edwards DA (1999) Estimating rate constants in a convection-diffusion system with a boundary reaction. IMA J Appl Math 63:89–112

Edwards DA (2001) The effect of a receptor layer on the measurement of rate constants. Bull Math Bio 63:301–327

Edwards DA (2011) Transport effects on surface reaction arrays: biosensor applications. Math Biosci 230:12–22

GE Healthcare (2006) Biacore Flexchip product information. Uppsala

GE Healthcare (2007) Label-free interaction analysis in real-time using surface plasmon resonance, (technology note 23)

Mason T, Pineda AR, Wofsy C, Goldstein B (1999) Effective rate models for the analysis of transport-dependent biosensor data. Math Biosci 159:123–144

Rich RL, Cannon MJ, Jenkins J, Pandian P, Sundaram S, Magyar R, Brockman J, Lambert J, Myszka DG (2008) Extracting kinetic rate constants from surface plasmon resonance array systems. Anal Biochem 373(1):112–120

Zumbrum M (2014) The effect of receptor nonuniformity for surface reactions within optical biosensors. IMA J Appl Math (submitted)